Article

A Deep Learning Approach to Improve the Control of Dynamic Wireless Power Transfer Systems

Manuele Bertoluzzo [1], Paolo Di Barba [2], Michele Forzan [1], Maria Evelina Mognaschi [2] and Elisabetta Sieni [3,*]

[1] Department of Industrial Engineering, University of Padua, 35131 Padua, Italy; manuele.bertoluzzo@unipd.it (M.B.); michele.forzan@unipd.it (M.F.)
[2] Department of Electrical, Computer and Biomedical Engineering, University of Pavia, 27100 Pavia, Italy; paolo.dibarba@unipv.it (P.D.B.); eve.mognaschi@unipv.it (M.E.M.)
[3] Department of Theoretical Applied Sciences, University of Insubria, 21100 Varese, Italy
* Correspondence: elisabetta.sieni@uninsubria.it

Abstract: In this paper, an innovative approach for the fast estimation of the mutual inductance between transmitting and receiving coils for Dynamic Wireless Power Transfer Systems (DWPTSs) is implemented. To this end, a Convolutional Neural Network (CNN) is used; an image representing the geometry of two coils that are partially misaligned is the input of the CNN, while the output is the corresponding inductance value. Finite Element Analyses are used for the computation of the inductance values needed for CNN training. This way, thanks to a fast and accurate inductance estimated by the CNN, it is possible to properly manage the power converter devoted to charge the battery, avoiding the wind up of its controller when it attempts to transfer power in poor coupling conditions.

Keywords: deep learning; dynamic wireless power transfer system; fast surrogate model; optimization; magnetic field; finite element analysis; field-circuit model

1. Introduction

Wireless Power Transfer (WPT) is a technology that uses magnetic coupling instead of classical plugs and cables to charge the onboard batteries of electric vehicles (EVs) [1–7]. In general, WPT systems (WPTSs) are based on a pair of coils, a transmitting (Tx) and a receiving (Rx) one, separated by an air gap [3,5,8–10]. Usually, the Tx coil is buried under a parking pitch while the receiving coil is fitted under the chassis of the vehicle, and the onboard battery is charged while the car is parked (static WPTS). Nowadays, dynamic WPTSs are an emerging method to charge a battery while a vehicle runs over suitable roads equipped with a set of transmitting coils under the ground [11,12]. In this case, depending on the car position, the Rx coil could be aligned, partially aligned, or misaligned with respect to the Tx one [13–16]. Then, it is important to investigate the variation in the mutual inductance considering different displacements from the fully aligned condition [13,17]. In fact, knowing the value of the mutual inductance for a given car position can be useful for actively controlling the WPTS, optimizing its efficiency, and maximizing transferred power [18].

In the past, the authors of this paper have studied WPTSs from different viewpoints, but this has never been performed in the field of mutual inductance estimation in view of WPTS control. They have studied the optimal synthesis of compensation networks for WPTS [15,18] and models for fast and accurate simulations of the magnetic field in WPTS; moreover, they investigated aspects related to the electromagnetic compatibility of these systems [16]. In this paper, a deep learning technique, which belongs to the more recent fields of research in electromagnetism, is exploited for optimizing transferred power in WPTSs.

In this paper, a fast method for identifying the mutual inductance of two misaligned coils at a given distance is proposed. This method, based on a Convolutional Neural Network (CNN), will allow the mutual inductance at each position of the Rx coil (and hence the car) to be predicted for any trajectory of the car. The mutual inductance is predicted by the CNN by processing an image that shows in real time the relative position of the T_X and R_X coils while the vehicle is running, and this is used for implementing real-time control of the power transfer for any trajectory of the vehicle moving over the Tx coil [19].

The CNN is a deep neural network able to effectively treat images and used to solve a classification or a regression problem. CNNs have been extensively used in the last decade by computer scientists for image processing (object detection, image segmentation, classification, etc.) [20]. However, it is only in the last few years that CNNs have been used for solving problems in electrical engineering and electromagnetism. In this frame, the use of CNN for the recognition of electrical machine faults is one of the most investigated fields of research [21].

In this paper, the innovative idea is to use a CNN to predict the value of the mutual inductance between the Tx and Rx coils based on their image. A CNN processes images generated by a camera mounted on the car bottom, which can catch the transmitting coil position thanks to its shape drawn on the road concrete. On the other hand, the shape and position of the Rx coil is known and, hence, its image can be superimposed to the one of the Tx coils. The resulting image is processed by the neural network, which solves a regression problem: the value of the mutual inductance between the Tx and Rx coils is predicted. Hence, the CNN is used for solving the following problem: knowing the image of the Rx and Tx coils and finding the value of the mutual inductance between them. The information on the coil shapes and on the relative position between the two coils is embedded in the image itself. The distance between the car bottom and the concrete is supposed to be constant; hence, the distance between the Tx and Rx coils in the z-direction is constant too.

The CNN is trained by means of a database of 3D Finite Element Analyses (FEAs). Once the CNN is trained, it is able to predict the mutual inductance between the two coils for any displacement between them, i.e., for any vehicle trajectory. To the best of the authors' knowledge, this approach is new in the field of dynamic Wireless Power Transfer. In the literature, similar approaches have been proposed recently, but they all refer to different applications or different machine learning methods. Indeed, there are a few papers dealing with Wireless Power Transfer based on the use of CNNs: these deep learning methods are usually applied to other kinds of usage or to different applications. In [22], a CNN is trained for estimating the overlapping area between a pot and a multi-coil system in the frame of domestic induction heating appliances: knowing the measured data for each coil (output power, current and quality factor), the area coverage is predicted using the CNN.

Papers dealing with WPTS propose the use of fully connected neural networks (NNs) (shallow or deep), which are different from CNNs and are able to treat numbers or a vector of numbers but not able to properly treat images. For the sake of an example, in [23], the estimation of the mutual inductance of a wireless power system is conducted by means of a neural network: a Bayesian neural network is used. This kind of network is able to predict the inductances of the WPTS by knowing the parameters of the system, i.e., geometrical and material parameters. A similar result is obtained in [24], where a deep NN accepts five structural parameters as the input to estimate the self- and mutual inductances of the coupled coils of a WPTS. In [25], a fully connected neural network is used for estimating the mutual inductance, knowing the distance between the two coils in a WPTS. However, with this approach, the distance must be measured, and this is not feasible in the case of dynamic WPTSs. In [26], a deep fully connected neural network is used for the WPTS parameter estimation based on the input current and the distance between the coils; this approach is not suitable for a dynamic WPTS. In [27], an NN is used to estimate the inductive parameters, the stray magnetic field, and the ferrite magnetic field of two coupled coils

using their geometrical characteristics as inputs. Paper [28] introduces the use of an NN to estimate the efficiency of a WPT system that encompasses an intermediate coil. The efficiency is estimated as a function of the resonance frequency and of the geometrical parameters of this coil. In [29], a similar layout is considered, but the NN is used to estimate the electromagnetic emission of the WPT system for a different layout of the intermediate coil. Paper [30] considers a biomedical application of WPT for transcutaneous power transfer and uses an NN to estimate the voltages, currents, and transferred power of the WPT using its geometrical data and coil distance as inputs. Paper [31] deals with the estimation of the inductive parameters of a circular coil and compares the estimates of an NN trained using data from the FEM with the analytical results derived from Neumann's formula. In [26], a similar topic is faced using the PyTorch framework to train the NN using data derived from simulations as inputs. The system considered in [32] is formed by the T_X and R_X coils and by four detection coils, whose induced voltage is processed by an NN to detect the presence of a foreign metallic object between the two main coils and to assess their relative displacement. None of these cited papers deal with dynamic WPTS, whilst most of them use data derived from the FEM simulations as the input. The processing of real-time data, whether in the form of images or not, is not considered.

Considering the control of the power converters, NNs have been used in the field of WPTSs for different purposes. In [33], a radial basis NN has been proposed to adjust the gains of a PID controller devoted to maintaining the resonant condition of the WPTS. An NN is also used to assess the gains of a PID controller in [34]; in this paper, the controller acts on the phase shift angle of the Rx side converter of a bidirectional WPTS. In [35], an NN is adopted with the aim of adjusting the supply frequency of the system, but in this case, the NN directly generates the required frequency value without an intermediate controller. Paper [36] faces the topic of maintaining a constant current on the WPTS load despite a variation in the coils' mutual inductance M. The NN is trained to assess the phase shift angle of the primary side high-frequency inverter as a function of the Tx coil current. In [37], the maximum power transfer efficiency in an underwater WPTS is maintained by adjusting the supply voltage according to the outputs of an NN. In [38], the efficiency of a WPT system is maximized by means of an NN that computes the optimal parameters for a tunable compensation network in order to enforce the impedance matching of the system despite a variation in the coils distance or in the load. The NN in [39] is used to estimate the orientation of the receiving coil with respect to the transmitting ones in an omnidirectional WPTS. Position estimation is also considered in [40], with the NN processing the signals coming from four auxiliary coils to assess the relative position of the coupled coils. The lateral misalignment between the Tx and Rx coils is estimated in [41] using an NN fed by the dc link current actual value, by its integrated value, and by the actual vehicle speed. In [42], the NN is used to select and enable the optimal transmitting coil among three available coils and to tune the relevant compensating capacitor using the distance between the transmitting and receiving coils as the input.

Considering the most recent papers published in the literature, the approach we propose in this paper seems not to have been investigated yet.

The remainder of this paper is organized as follows. In Section 2, the WPTS model is described: the circuit model and the Finite Element (FE) model are presented, along with the control strategy. Moreover, in Section 2.3, the deep learning strategy is described. In Section 3, the results are shown: in Section 3.1, the outcome of CNN training is discussed, and in Section 3.2, the results of the control strategy, based on the trained CNN, are shown. Finally, in Section 4, a conclusion is drawn.

2. WPTS Model

Finite Element Analysis is used to compute the lumped parameters used in a circuital model for the supply control of the transmitting coil in a WPTS for the recharge of an electric vehicle.

2.1. Lumped Parameter WPTS Model

The lumped parameter first harmonic equivalent circuit of the WPTS is represented in Figure 1. In the transmitting side, the Tx coil is supplied by the voltage $\overline{V}_S$ through an LCL compensation network. This topology has been adopted in order to have a current with a constant amplitude in the T_X coils irrespective of the actual reflected load. The compensation network is formed by the inductor L_S and the capacitor C_{Tx}. The inductance L_S is equal to the self-inductance of L_{Tx} of the transmitting coil and C_{Tx} resonated with both of them. The resistance R_S accounts for the parasitic resistances of L_S and of the voltage generator, while R_{Tx} represents the parasitic resistance of the T_X coil. The T_X coil is flown by the current $\overline{I}_{Tx}$ and is subjected to the induced voltage $j\omega M \overline{I}_{Rx}$, which is proportional to the amplitude of the current $\overline{I}_{Rx}$ in the receiving coil, to the WPTS supply angular frequency ω, and to the mutual inductance M between the T_X and R_X coils, which is inherently variable in time. At the R_X side, a series compensation network formed by the capacitor C_{Rx} that resonates with the self-inductance of L_{Rx} of the R_X coil has been chosen so that the full voltage $-j\omega M \overline{I}_{Tx}$ induced across the R_X coil is available to charge the battery. The resistor R_{Rx} represents the parasitic resistance of the R_X coil, while R_L represents the equivalent load of the system. Following the SAE standard [11], the WPTS is supplied by a voltage oscillating at 85 kHz so that the current flowing in the T_X induces a voltage with the same frequency across the R_X coil.
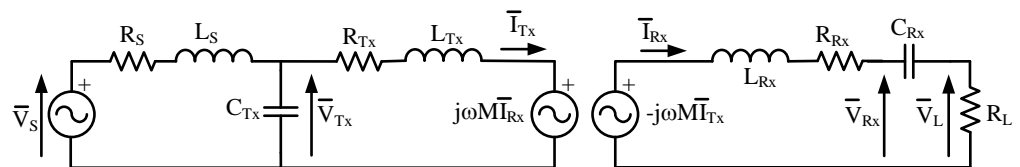

Figure 1. WPTS with LCL-series topology.

2.2. Field Model of WPTS for Database Creation: Finite Element Analysis

In order to train the CNN for the mutual inductance estimation, a 3D Finite Element Model (FEM) is set up. Figure 2 represents the pair coils simulated in the FEM to compute their mutual inductance at different positions of the Rx coil with respect to the Tx coil. Each coil is formed by 10 turns having a pitch of 10 mm and a wire diameter of 6 mm; the width of the inductor is 106 mm. The vertical distance between the coils is set to 200 mm. The mesh of the FEM has 832,251 nodes and 619,680 s order volume elements.
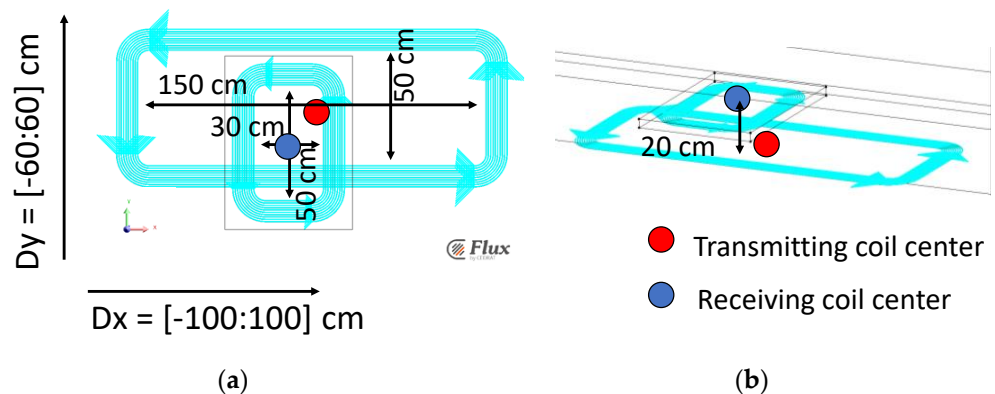

Figure 2. Geometry of the model used in FEA: (**a**) XY section with coil size and (**b**) 3D with vertical distance.

The FEA solves a time-harmonic magnetic field problem using Flux 3D version 12.1 (software released by Altair Engineering, Inc., Troy, MI, USA, https://altairhyperworks.com/product/flux, accessed on 28 November 2023). The model is simple since it considers an air volume where the coils are described as ideal sources of the magnetic field without

discretization (non-meshed coils). In this frame, the magnetic field produced by the coils is evaluated in a semi-analytical way using the Biot–Savart formula [43], whereas in the air volume, a reduced scalar magnetic potential, Φ_R, formulation is applied [44,45]:

$$\nabla \cdot \mu_0 \boldsymbol{H}_s = \nabla \cdot \mu_0 \nabla \Phi_R \tag{1}$$

$$\boldsymbol{H} = \boldsymbol{H}_s - \nabla \Phi_R \tag{2}$$

where $\boldsymbol{H}$ is the magnetic field, μ_0 is the vacuum magnetic permeability, and $\boldsymbol{H}_s$ is the magnetic field generated by the coil and computed using the Biot–Savart law.

A typical magnetic flux density map for three different Rx coil positions is shown in Figure 3 in terms of an arrow plot of the B vector. The magnetic flux density is visualized in a xz plane with y = 0, where x = 0 and y = 0 corresponds to the aligned coil case. In Figure 3a, a perfectly aligned case is represented; Figure 3b corresponds to a particular position of the R_X coil where it is partially overlapped to the T_X coil but, nevertheless, it is flown by a null net flux generated by $\bar{I}_{Tx}$ and, consequently, the mutual coupling M is equal to 0. Figure 3c corresponds to the coils superposed only on a corner.
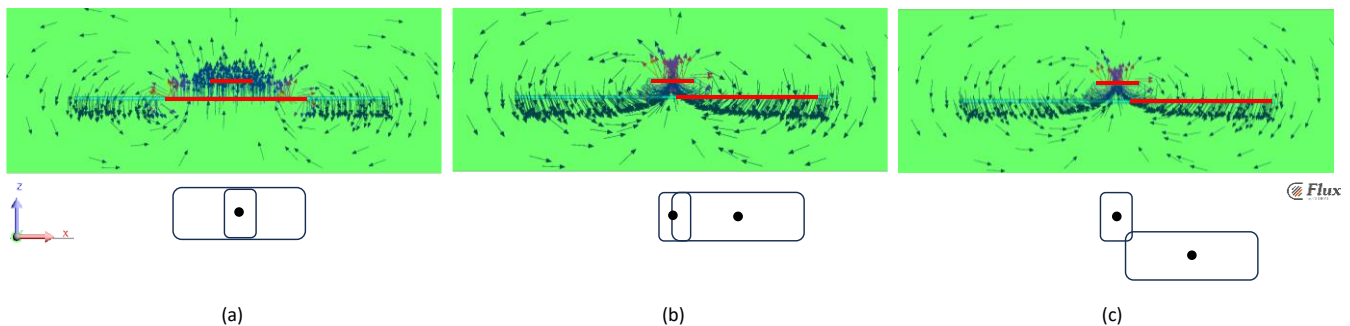

Figure 3. Arrows plot of magnetic flux density (**a**) centered inductor, (**b**) inductors positioned in order to have M = 0, and (**c**) superposition on a corner. Red lines represent the coil position in XZ plane and black rectangles the coil position in XY plane.

To evaluate the lumped parameters, i.e., self- and mutual inductance, the electromagnetic model was coupled to an electric circuit [17,46].

The Rx coil was moved on a (Dx, Dy) grid with the origin on the center of the Tx and ranging from −100 cm to 100 cm in the x direction and from −60 cm to 60 cm in the y direction, as depicted in Figure 2a. The worst case considered for misalignment is Dx = 100 mm and Dy = 60 mm; in this case, a 117 mm × 112 mm area of overlapping takes place. Because the coil width is 106 mm, in the worst case, the overlap between the two coils occurs in the copper areas. This case, as well as all the cases where a strong misalignment occurs, cannot be properly treated with analytical formulations for the mutual inductance calculation because the accuracy of the analytical methods strongly depends on the level of misalignment. In general, the stronger the misalignment, the worse the accuracy of the mutual inductance evaluation. However, thanks to the use of 3D FE field analysis, the fringing field effect is well simulated, even in the case of substantial misalignment of the coils.

Figure 4 represents the mutual inductance as a function of the Dx shift in the range from 0 cm to 100 cm for different values of Dy chosen in the range from 0 cm to 60 cm. The mutual inductance M obtained from the FEA ranges from −2.2 μH to 19.9 μH. The self-inductances are unaffected by the relative position of the coils and are equal to 245 μH and 81.9 μH for the Tx and Rx coils, respectively.
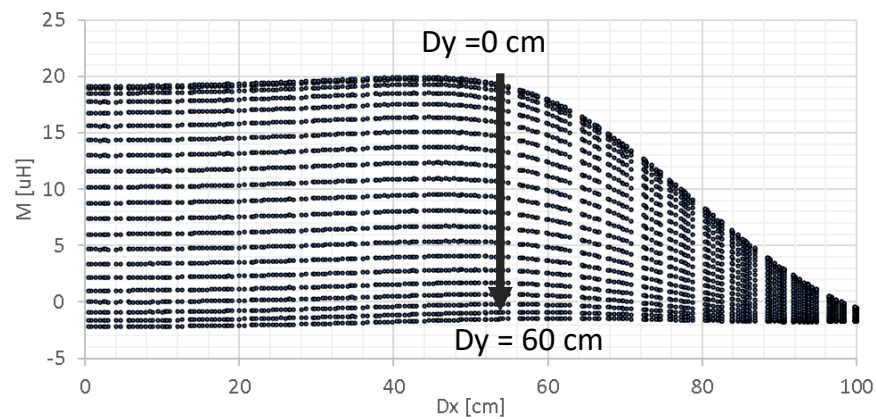
Figure 4. Mutual inductance in one quarter of the model. Black arrow represents the effect of Dy increment.

The database of solutions is composed of 5000 random samples. The images of the coils in different positions are generated using Matlab version 2021a, as represented in Figure 5. Each image is saved in .jpeg format with a resolution of 1200 DPI and converted to a black and white figure with a given resolution suitable for the Neural Network. In particular, the resolution is reduced more and more, and for each resolution, the image quality is checked; no holes in nor missing parts of the conductors should be in the image. The lower resolution, which allows a good image quality (no loss of information), is 100×120 pixels. Then, each sample is composed of a simplified black and white image of the two coils (100×120 pixels), as shown in Figure 5b and by the corresponding mutual inductance value.
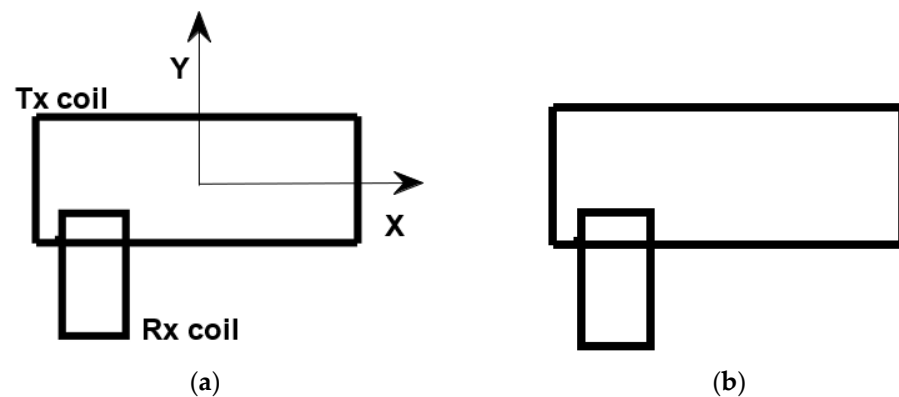
Figure 5. Geometry of the system (**a**); image for the CNN input (**b**).

The image is a black and white image of size 100×120 pixels (Figure 5b).

2.3. CNN-Based Approach

For predicting the mutual inductance, a CNN is used [47]. The CNN is composed of 27 layers, as shown in Table 1.

The input is a matrix 100×120 (the image of the coils), and one value is the output (mutual inductance). The image resolution has been set up as a trade-off between the accuracy in the representation of image details and the lowest resolution. In fact, the image resolution is usually a critical parameter because the lower the resolution image, the better the CNN training with a given dataset of images, but, on the other hand, no loss of information is wanted.

During CNN training, the database is used as follows: batches of coil images are given one by one as the input to the CNN, characterized by a set of weights, as previously initialized. At each iteration, the predicted value of mutual inductance is compared to

the true value, given by the database, and an error (usually the Root Mean Square Error, RMSE) is calculated. From batch to batch, the weights of the CNN are updated based on the chosen optimization algorithm, e.g., the Adaptive Moment Estimation (ADAM) in our case, and when the maximum number of iterations is reached or a prescribed tolerance is met, the training stops.

Table 1. CNN architecture.

Layers	Layers
(1) Image-based input (size $100 \times 120 \times 1$)	(15) Batch normalization
(2) Convolution 2D (size 3×8),	(16) ReLU activation function
(3) Batch normalization	(17) Average pooling layer (size 2×2)
(4) ReLU activation function	(18) Convolution 2D (size 3×128)
(5) Average pooling layer (size 2×2)	(19) Batch normalization
(6) Convolution 2D (size 3×16)	(20) ReLU activation function
(7) Batch normalization	(21) Average pooling layer (size 2×2)
(8) ReLU activation function	(22) Convolution 2D (size 3×256)
(9) Average pooling layer (size 2×2)	(23) Batch normalization
(10) Convolution 2D (size 3×32)	(24) ReLU activation function
(11) Batch normalization	(25) Dropout (40% probability)
(12) ReLU activation function	(26) Fully connected layer (1 output)
(13) Average pooling layer (size 2×2)	(27) Regression layer
(14) Convolution 2D (size 3×64),	

Hence, for the supervised training procedure, the problem reads as follows: given the database of images and relevant mutual inductance values, the network weights are found by minimizing the error between the predicted and prescribed output according to the selected algorithm.

In turn, the trained CNN is then used to solve the following problem: given an un-previously seen image of the two coils as input, find the mutual inductance value utilizing the trained CNN.

As far as the CNN architecture is concerned, it is possible to highlight some recurrent sequence of layers: each sequence is composed of an average pooling layer, a convolutional layer, a batch normalization layer [48], and a Rectified Linear Unit (ReLU) function (see Table 1).

The ReLU function is one of the most used activation functions for the CNN because it has shown good performance in training this kind of neural network in terms of avoiding overfitting [47]. The convolutional layers are characterized by filters sized 3×3. The number of filters varies from 8 to 256. In order to obtain a more stable solution, average pooling layers with a filter sized 2×2 are applied. At the end of the CNN, a dropout layer is used, and a fully connected layer followed by the regression layer allows for one element to be obtained as the output of the neural network.

The CNN was trained with 80% of database samples for training and 20% for validation, i.e., 4000 samples for the training set and 1000 samples for the validation set. The CNN was trained with the Adaptive Moment Estimation (ADAM) method with the following hyper-parameter values: mini-batch size 128, initial learning rate 10^{-4}, learning rate drop factor 0.9, and learning rate drop period 20.

The tuning of the hyper-parameters is conducted by means of a trial-and-error procedure: the highest sensitivity of the CNN training is given by the initial learning rate. By increasing the initial learning rate, training can occur faster, but a local minimum of the weights optimization can occur as well as divergent behavior during the training; this results in non-accurate training. On the other hand, if the initial learning rate is too small, the training is very long. The best value of the initial learning rate depends also on the CNN architecture. For our problem, we found that the best value is 10^{-4}.

For evaluating the quality of the CNN-based prediction, the Mean Average Percentage Error MAPE (%) was calculated considering the N points of the validation set, namely, in percentage:

$$\text{MAPE} = 100 \frac{1}{N} \sum\nolimits_{i=1}^{N} \frac{\left| \hat{Y}_i - Y_i \right|}{|Y_i|} \tag{3}$$

where Y is the true value calculated analytically, and $\hat{Y}$ is the value predicted by the CNN. Another figure of merit for evaluating the CNN performance is the Root Mean Square Error (RMSE):

$$\text{RMSE} = \sqrt{\sum\nolimits_{i=1}^{N} \frac{\left(\hat{Y}_i - Y_i \right)^2}{N}} \tag{4}$$

The MAPE error was preferred in this paper because it has an easy interpretation, and it is expressed as a percentage. When the outliers (points with large error) are to penalize, the RMSE is preferred because it increases when the number of outliers increases.

2.4. Control Strategy

Figure 6 gives a more detailed representation of the WPTS. The main difference with respect to Figure 1 is in the R_X side of the system, where the equivalent load R_L has been split into its main components. Indeed, this is formed by the cascade of a diode rectifier, a buck chopper, a filter inductance, and, finally, by the battery to be charged.
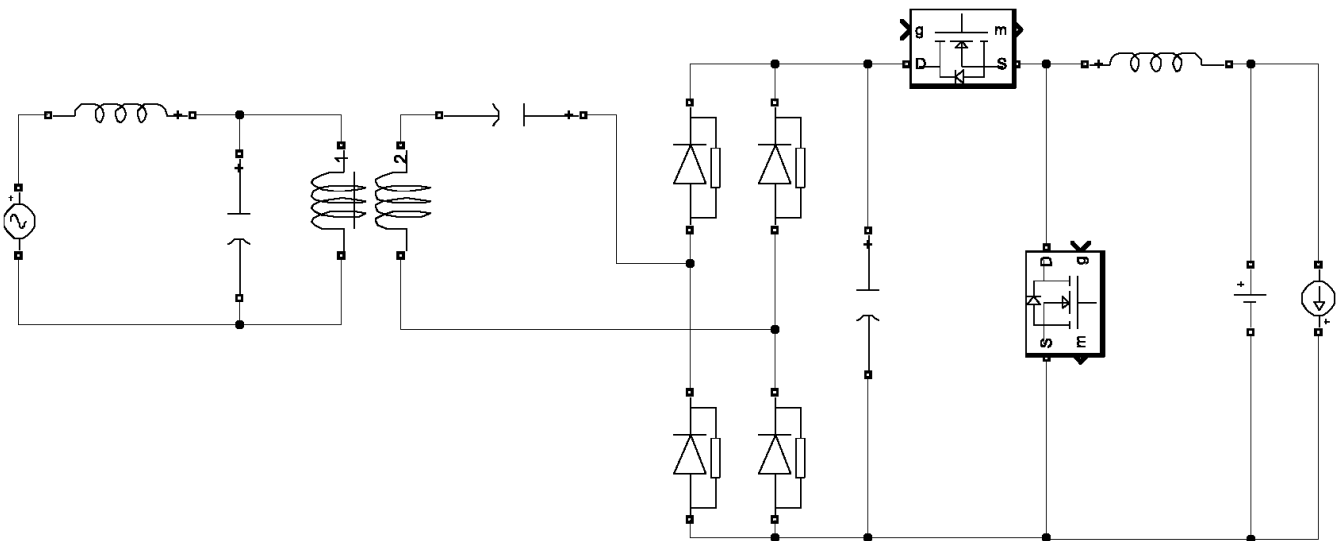

Figure 6. Scheme of the dynamic WPTS equivalent circuit.

Thanks to the LCL compensation, the current flowing in the Tx coil depends only marginally on the actual values of the power injected in the battery and of M, so that it can be considered as a given parameter of the system. Consequently, it is possible to design the control algorithm focusing only on the R_X side of the WPTS.

Battery charging is controlled by means of two nested loops. The outer loop controls the battery voltage and, by processing the voltage reference and the actual voltage, works out the reference for the current to be injected in the battery. The inner loop processes the current reference and generates command signals for power switches of the chopper.

Obviously, when the coupling between the T_X and R_X coils is very low or when the coils are not coupled at all, no power transfer can be performed, and the controller of the abovementioned control loops saturates. When the vehicle moves and the coils are coupled again, the saturated controllers cause unwanted overshoot on the battery-charging current. These unwanted solicitations are avoided by exploiting the estimate of M computed by the CNN. When it is too low to the power, transfer is considered unfeasible, and the outer loop

controller sets the charging current reference to zero. When the estimate M is high enough, the current reference is updated in order to go on with the battery charging.

3. Results

The CNN was trained using the database obtained by means of FEAs. The trained CNN was used in the control of the WPTS, with a focus on properly managing the transition from couple to uncoupled conditions and vice versa.

3.1. CNN Training

The CNN training progress recorded for 500 epochs is shown in Figure 7.
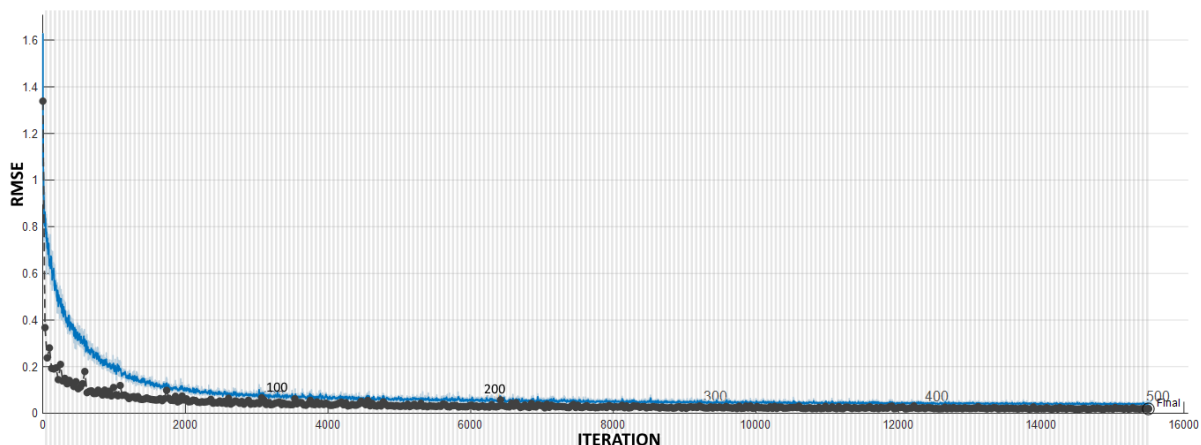

Figure 7. Training progress of the CNN. Blue—RMSE of the training set; black—RMSE of the validation set.

At the end of the training procedure, the RMSE is low for both the validation and training sets.

The MAPE error of the CNN trained for 500 epochs is equal to 16%. Because the MAPE error formula has the true value of the mutual inductance at the denominator, the highest MAPE errors are given for mutual inductance values close to zero.

Another way of showing the quality of the results is to plot the true values of the mutual inductance versus the predicted values for the validation set. The solutions of the validation set obtained with the FEM versus those predicted by the trained CNN are shown in Figure 8.
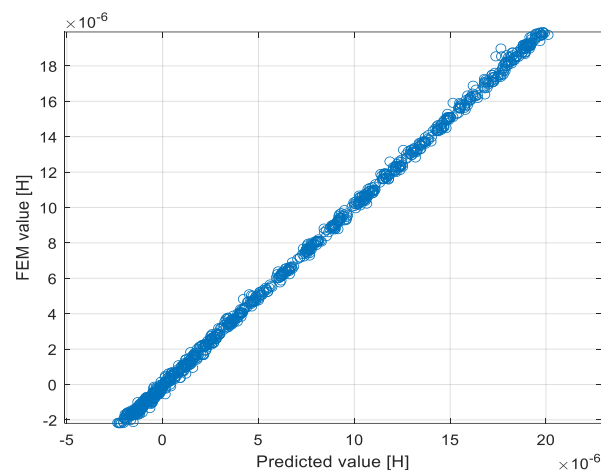
Figure 8. True vs. predicted values of mutual inductance.

The closer the points to the bisector line, the better the accuracy of the neural network prediction. As shown in Figure 8, the points are located along the bisector with good accuracy.

In Figure 9, the prediction of the mutual inductance versus the coil misalignment for two test cases (linear and V-shaped trajectory) is shown.
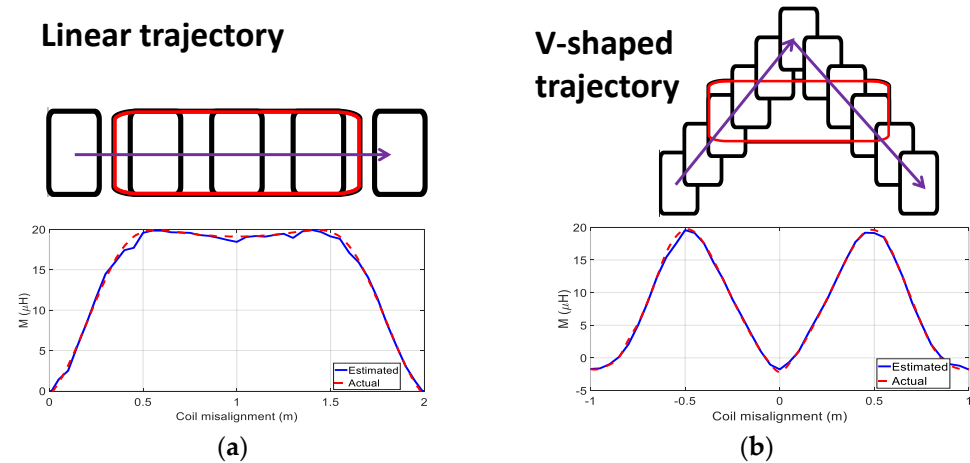
Figure 9. Linear (**a**) and V-shaped (**b**) trajectories and relevant estimated and actual mutual inductances. Red rectangle represents the inductor on the road and purple arrows the car trajectory.

In both cases, the value of the mutual inductance is predicted with acceptable accuracy, and the maximum prediction errors can be recognized to happen in correspondence with the maximum values of M. As it will be explained in the following section, this characteristic does not impair the effectiveness of the algorithm that manages the battery charging. Figure 9a, relevant to the liner trajectory, shows the same profile of M reported in Figure 4. Along the V-shaped trajectory, considered in Figure 9b, the R_X coil moves twice from the misaligned to the aligned condition while the EV passes on one T_X coil. For this reason, the profile of M exhibits two rounded peaks instead of a flat top like in Figure 9a.

3.2. Battery Charging

The CNN trained as described in Section 3.1 was used in the control strategy that manages the battery charging according to the approach described in Section 2.4. Two different trajectories have been used: the linear one and the V-shaped one (see Figure 9).

3.3. Linear Trajectory

When the EV follows a linear trajectory, the induced voltage v_r has the waveform reported in Figure 10 with the blue line.
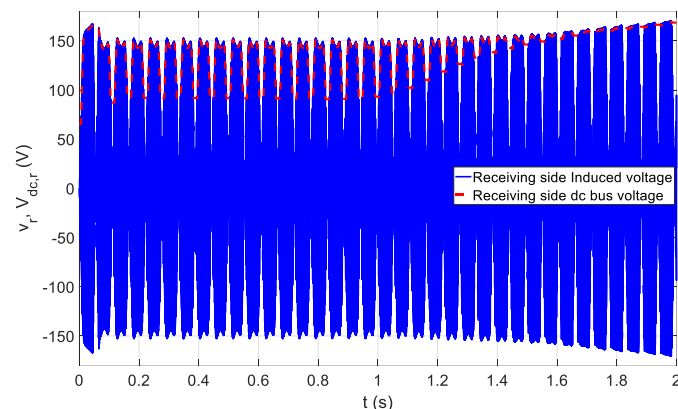
Figure 10. Induced voltage v_r (solid blue) and dc bus voltage $V_{dc,r}$ (dashed red). Linear Trajectory.

The figure refers to an EV running at a constant speed of 130 km/h and considers a time span of 2 s, during which the EV meets 35 Tx coils. Because of the high supply frequency of the Tx coils, the oscillations of v_r are too fast to be resolved at the time scale of the figure and only the envelope of the induced voltage can be recognized. The dashed red line in the figure represents the receiving side dc bus voltage. As shown in Figure 6, it is obtained as the output of a diode rectifier processes the induced voltage and charges the dc bus capacitor. For this reason, the dc bus voltage follows the envelope of the induced voltage but is a little lower because of the voltage drop across the diodes. At the same time, a buck chopper discharges the capacitor and injects in the battery the power coming from the Tx coils. On its turn, the battery supplies the traction drive of the vehicle, which is represented in Figure 6 by a constant current generator.

The control algorithm of the chopper is designed to charge the battery following the current reference represented by the red dashed line of Figure 11. It is saturated to the maximum battery-charging current when the battery voltage is much lower than the reference one, thus implementing the constant current charging stage, and then decays slowly to zero while the battery voltage approaches the reference value.
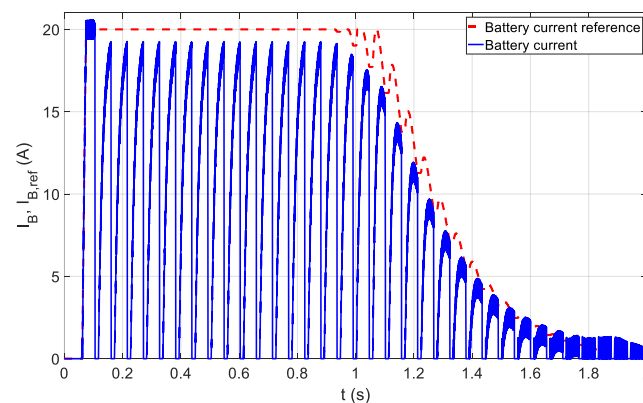
Figure 11. Battery-charging current reference $I_{B,ref}$ (dashed red) and actual charging current I_B (solid blue).

This current can be drawn from the dc bus capacitor only if the diode rectifier is in the conduction state, otherwise the capacitor voltage decreases below the battery voltage and the chopper does not work anymore. In this condition, the current controller must be disabled in order to avoid its windup and the consequent current overshoot as soon as enough voltage is again available.

Considering that the amplitude of v_r is proportional to M, the estimated M computed by the CNN is used to enable and disable the current controller and the chopper operations. In particular, when the estimated M is lower than 45% of its nominal value M_N, the chopper is disabled, and the current reference is kept constant. When M exceeds 50% of M_N, the controller and the chopper are enabled again. The 5% hysteresis between disabling and enabling the controller avoids undue commutation between the two working conditions during the vehicle run.

In order to speed up the simulations used to test the performance of overall dynamic WPTS, the battery has been substituted for a large capacitor, and the load current has been set to zero. In this way, a simulation time of 2 s is enough to check all the working conditions of the systems.

Figure 11 shows that at the beginning of the charging process, $I_{B,ref}$ saturates to its maximum value. After about 1 s, it exits from saturation and decreases down to zero at the end of the simulation time. Due to the high speed of the vehicle, the battery current I_B does not reach $I_{B,ref}$ within the time taken by the vehicle to move over a single T_X coil. Instead, I_B is forced to zero every time M falls below 45% of M_N and the chopper is disabled.

The current I_B restarts flowing when the power transfer from the next transmitting coil is enabled again, and a new partial charge of the battery is performed.

When $I_{B,ref}$ decreases, the duration of the coupling with a single T_X coil becomes enough to allow I_B to approach $I_{B,ref}$, as it can be recognized in Figure 11 in the time interval from about 1.2 s to 2 s. This behavior is highlighted in Figure 12, which reports a magnification of Figure 11.
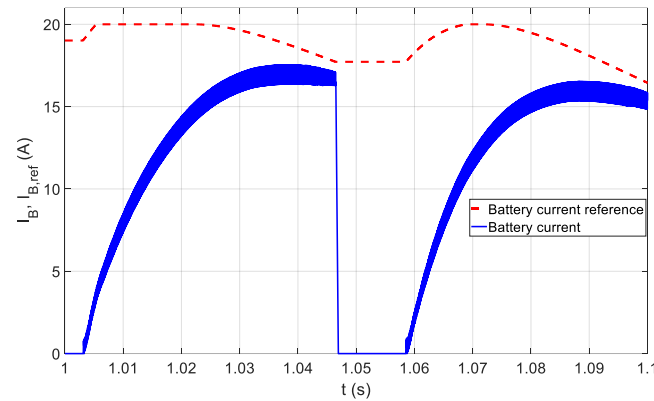
Figure 12. Battery-charging current reference $I_{B,ref}$ (dashed red) and actual charging current I_B (solid blue). Linear Trajectory.

It clearly shows that neither $I_{B,ref}$ nor I_B are subject to overshot and that $I_{B,ref}$ is kept constant while I_B is forced to zero. The oscillations of $I_{B,ref}$ are due to the repeated enabling and disabling of the power transfer. For time longer than 1.6 s, $I_{B,ref}$ is even lower and I_B reaches it within the duration of a coupling with a single T_X coil, as shown in Figure 11.

The current I_B is forced to zero and the chopper is disabled while M is decreasing. This means that the amplitude of the induced voltage v_r is decreasing as well and given that the dc bus capacitor is not discharged by the chopper, the diodes of the rectifier are inversely polarized. In these conditions, $V_{dc,r}$ does not follow anymore v_r but is kept constant to the value it had when the chopper was disabled. This behavior is confirmed by Figure 13, which is a magnification of Figure 10 relevant to the same time interval as Figure 12.
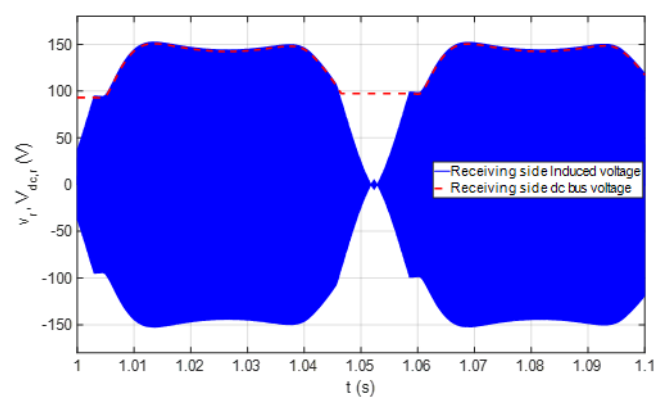

Figure 13. Induced voltage v_r (solid blue) and dc bus voltage $V_{dc,r}$ (dashed red). Linear Trajectory.

The figure confirms that the amplitude of v_r, represented by the blue solid shape, follows the profile of M shown in Figure 4. Between the two Tx coils, $V_{dc,r}$, represented by the red dashed line, is constant. It starts following the envelope of v_r as soon as the peak of v_r exceeds $V_{dc,r}$ and the diode rectifier conducts again.

Despite the intermittent power transfer, the battery is actually charged, and its voltage increases up to the end-of-charge reference value. This is confirmed by Figure 14 that reports the behavior of the battery voltage starting from the initial value of 54 V to the full

load value of 56 V. The stepped profile is due to the subsequent chopper turning on and off. Indeed, the battery voltage increases while the chopper injects current on it and stays constant while the chopper is off.
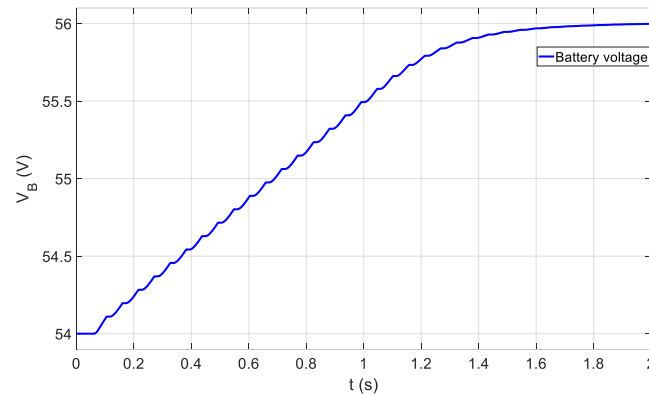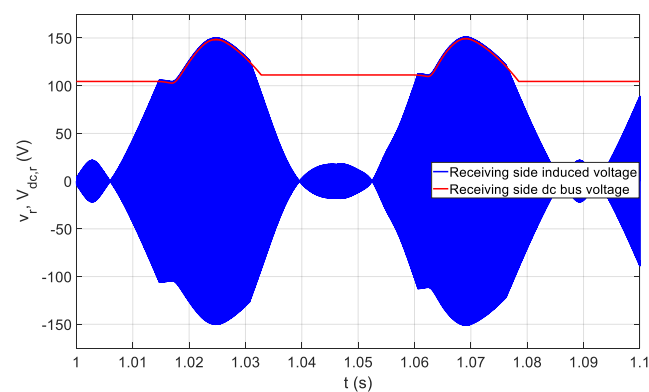

Figure 14. Battery voltage. Linear Trajectory.

3.4. V-Shaped Trajectory

In the V-shaped trajectory, M has the profile shown in Figure 9b. Even if it is not realistic for a driver to follow such a profile, this case has been studied to check the robustness of the estimates coming from the NN and of the control algorithm that exploits them to charge the vehicle battery. As in the previous case, the vehicle speed has been considered equal to 130 km/h. However, because of the longer path to travel over each Tx coil, the vehicle meets only 25 Tx coils in 2 s. In this time span, the profile of the induced voltage is not clearly distinguished from that one reported in Figure 11, relevant to the linear trajectory.

In order to appreciate the differences between the two trajectories it is necessary to examine the induced voltage profile considering a shorter time interval, as in Figure 15.


Figure 15. Induced voltage v_r (solid blue) and dc bus voltage $V_{dc,r}$ (solid red). V-Shaped Trajectory.

It should be compared with Figure 13, which is relevant to the linear trajectory and considers the same time interval. In this interval, the vehicle running on the linear trajectory meets two Tx coils, each of the originating one of the two blue solid spots in Figure 13. In the same time interval, the vehicle running on the V-shaped trajectory meets only one Tx coil, but, as shown in Figure 9b, the mutual inductance M between this Tx coil and the Rx coil exhibits two maxima. Consequently, Figure 15 reports two solid spots, like Figure 13, both originated by the same Tx coil. The smaller spot laying in the 1.04 s–1.05 s time interval corresponds to the condition of having M negative but with a non-negligible value. Also in this case, the red line in Figure 15 represents the dc bus voltage $V_{dc,r}$.

The presence of a large interval in which the induced voltage is rather low reduces the time available to enable the buck chopper to charge the battery. Indeed, as shown by the dashed red line in Figure 15, the dc bus voltage remains constant for most of the time.

The reference for the current charging the battery and its actual value are plotted in Figure 16. It clearly appears that the current flows for a much shorter time interval with respect to Figure 12, and that its maximum value is sensibly lower than the one reached along the linear trajectory.
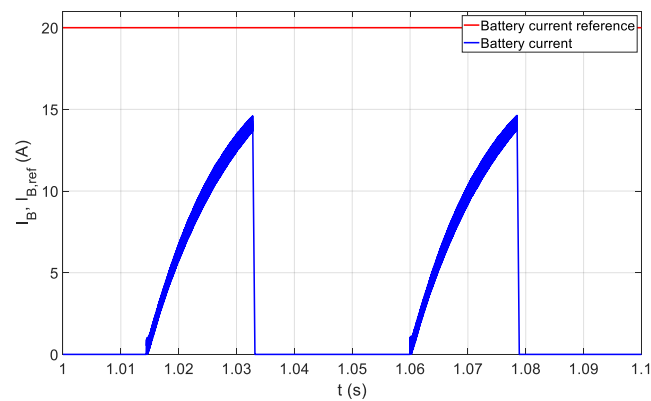
Figure 16. Battery-charging current reference $I_{B,ref}$ (solid red) and actual charging current I_B (solid blue). V-Shaped Trajectory.

Figure 17 shows that, despite this limitation, the battery can still be charged, even if the increasing rate of its voltage is more than two times lower than the one obtained in the linear trajectory.
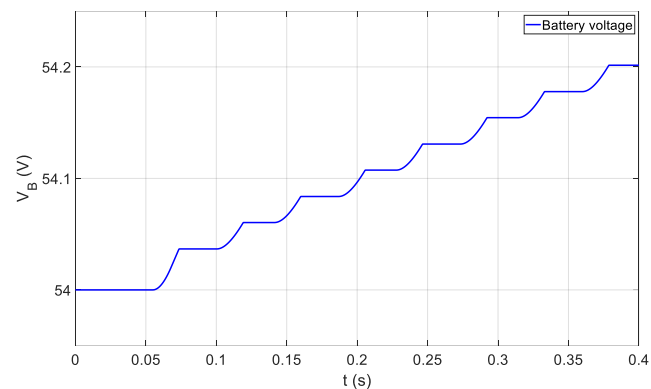
Figure 17. Battery voltage. V-Shaped Trajectory.

4. Conclusions

The proposed deep learning method for the fast estimation of the mutual inductance between two coils in a DWPTS shows a rather good accuracy and allows for the implementation of the control of the power converter for the battery charge.

Being based on the image of the two coils, this approach is suitable for an early prediction of the mutual inductance before the Rx coil is aligned with the Tx coil if the camera can capture the image of the forthcoming transmitting coil.

Finally, this method could also be used on the Tx side, considering a camera buried in the ground, for the control of the power supply. Hence, the proposed approach is general and could improve DWPTSs from different points of view.

Author Contributions: Conceptualization, M.E.M. and P.D.B.; methodology, M.E.M., E.S. and M.B.; validation, E.S. and M.B.; formal analysis, M.E.M. and M.F.; investigation, M.E.M., E.S. and M.B.; data curation, M.E.M., E.S. and M.B.; writing—original draft preparation, M.E.M., E.S. and M.B.;

References

1. Cirimele, V.; Diana, M.; Freschi, F.; Mitolo, M. Inductive Power Transfer for Automotive Applications: State-of-the-Art and Future Trends. *IEEE Trans. Ind. Appl.* **2018**, *54*, 4069–4079. [CrossRef]
2. Choi, S.Y.; Gu, B.W.; Jeong, S.Y.; Rim, C.T. Advances in Wireless Power Transfer Systems for Roadway-Powered Electric Vehicles. *IEEE J. Emerg. Sel. Top. Power Electron.* **2015**, *3*, 18–36. [CrossRef]
3. Triviño, A.; González-González, J.M.; Aguado, J.A. Wireless Power Transfer Technologies Applied to Electric Vehicles: A Review. *Energies* **2021**, *14*, 1547. [CrossRef]
4. Kindl, V.; Frivaldsky, M.; Zavrel, M.; Pavelek, M. Generalized Design Approach on Industrial Wireless Chargers. *Energies* **2020**, *13*, 2697. [CrossRef]
5. Tan, L.; Zhang, M.; Wang, S.; Pan, S.; Zhang, Z.; Li, J.; Huang, X. The Design and Optimization of a Wireless Power Transfer System Allowing Random Access for Multiple Loads. *Energies* **2019**, *12*, 1017. [CrossRef]
6. Feng, H.; Tavakoli, R.; Onar, O.C.; Pantic, Z. Advances in High-Power Wireless Charging Systems: Overview and Design Considerations. *IEEE Trans. Transp. Electrific.* **2020**, *6*, 886–919. [CrossRef]
7. Liang, C.; Yang, G.; Yuan, F.; Huang, X.; Sun, Y.; Li, J.; Song, K. Modeling and Analysis of Thermal Characteristics of Magnetic Coupler for Wireless Electric Vehicle Charging System. *IEEE Access* **2020**, *8*, 173177–173185. [CrossRef]
8. Li, S.; Mi, C.C. Wireless Power Transfer for Electric Vehicle Applications. *IEEE J. Emerg. Sel. Top. Power Electron.* **2015**, *3*, 4–17. [CrossRef]
9. Yakala, R.K.; Pramanick, S.; Nayak, D.P.; Kumar, M. Optimization of Circular Coil Design for Wireless Power Transfer System in Electric Vehicle Battery Charging Applications. *Trans Indian Natl. Acad. Eng.* **2021**, *6*, 765–774. [CrossRef]
10. Winges, J.; Rylander, T.; Petersson, C.; Ekman, C.; Johansson, L.-A.; McKelvey, T. Multi-Objective Optimization of Wireless Power Transfer Systems with Magnetically Coupled Resonators and Nonlinear Loads. *PIER B* **2019**, *83*, 25–42. [CrossRef]
11. *J2954_202010*; Wireless Power Transfer for Light-Duty Plug-in/Electric Vehicles and Alignment Methodology. SAE International: Warrendale, PA, USA, 2020.
12. Bavastro, D.; Canova, A.; Cirimele, V.; Freschi, F.; Giaccone, L.; Guglielmi, P.; Repetto, M. Design of Wireless Power Transmission for a Charge While Driving System. *IEEE Trans. Magn.* **2014**, *50*, 965–968. [CrossRef]
13. Di Capua, G.; Femia, N.; Stoyka, K.; Di Mambro, G.; Maffucci, A.; Ventre, S.; Villone, F. Mutual Inductance Behavioral Modeling for Wireless Power Transfer System Coils. *IEEE Trans. Ind. Electron.* **2021**, *68*, 2196–2206. [CrossRef]
14. Di Capua, G.; Maffucci, A.; Stoyka, K.; Di Mambro, G.; Ventre, S.; Cirimele, V.; Freschi, F.; Villone, F.; Femia, N. Analysis of Dynamic Wireless Power Transfer Systems Based on Behavioral Modeling of Mutual Inductance. *Sustainability* **2021**, *13*, 2556. [CrossRef]
15. Bertoluzzo, M.; Di Barba, P.; Dughiero, F.; Mognaschi, M.E.; Sieni, E. Multicriterion Synthesis of an Electric Circuit for Wireless Power Transfer Systems. *Przegląd Elektrotechniczny* **2020**, *96*, 188–192. [CrossRef]
16. Bertoluzzo, M.; Di Barba, P.; Forzan, M.; Mognaschi, M.E.; Sieni, E. Field Models for the Electromagnetic Compatibility of Wireless Power Transfer Systems for Electric Vehicles. *Eng. Comput.* **2022**, *37*, 2802–2819. [CrossRef]
17. Bertoluzzo, M.; Di Barba, P.; Forzan, M.; Mognaschi, M.E.; Sieni, E. Finite Element Models of Dynamic-WPTS: A Field-Circuit Approach. *COMPEL—Int. J. Comput. Math. Electr. Electron. Eng.* **2022**, *41*, 1146–1158. [CrossRef]
18. Bertoluzzo, M.; Di Barba, P.; Forzan, M.; Mognaschi, M.E.; Sieni, E. Optimization of Compensation Network for a Wireless Power Transfer System in Dynamic Conditions: A Circuit Analysis Approach. *Algorithms* **2022**, *15*, 261. [CrossRef]
19. Zhou, Z.; Zhang, L.; Liu, Z.; Chen, Q.; Long, R.; Su, H. Model Predictive Control for the Receiving-Side DC–DC Converter of Dynamic Wireless Power Transfer. *IEEE Trans. Power Electron.* **2020**, *35*, 8985–8997. [CrossRef]
20. Alzubaidi, L.; Zhang, J.; Humaidi, A.J.; Al-Dujaili, A.; Duan, Y.; Al-Shamma, O.; Santamaría, J.; Fadhel, M.A.; Al-Amidie, M.; Farhan, L. Review of Deep Learning: Concepts, CNN Architectures, Challenges, Applications, Future Directions. *J. Big Data* **2021**, *8*, 53. [CrossRef]
21. Jiao, J.; Zhao, M.; Lin, J.; Liang, K. A Comprehensive Review on Convolutional Neural Network in Machine Fault Diagnosis. *Neurocomputing* **2020**, *417*, 36–63. [CrossRef]
22. Guillen, P.; Fiedler, F.; Sarnago, H.; Lucia, S.; Lucia, O. Deep Learning Implementation of Model Predictive Control for Multioutput Resonant Converters. *IEEE Access* **2022**, *10*, 65228–65237. [CrossRef]
23. Sato, K.; Kanamoto, T.; Kudo, R.; Hachiya, K.; Kurokawa, A. Bayesian Neural Network Based Inductance Calculations of Wireless Power Transfer Systems. *IEICE Electron. Express* **2023**, *20*, 20230030. [CrossRef]

24. Sato, K.; Kanamoto, T.; Kudo, R.; Hachiya, K.; Kurokawa, A. Deep Neural Network Based Inductance Calculations of Wireless Power Transfer Systems. In Proceedings of the 2022 IEEE 11th Global Conference on Consumer Electronics (GCCE), Osaka, Japan, 18 October 2022; pp. 222–223.

25. He, L.; Zhao, S.; Wang, X.; Lee, C.-K. Artificial Neural Network-Based Parameter Identification Method for Wireless Power Transfer Systems. *Electronics* **2022**, *11*, 1415. [CrossRef]

26. He, S.; Xiao, J.; Tang, C.; Wu, X.; Wang, Z.; Li, Y. Load and Self/Mutual Inductance Identification Method of LCC-S WPT System Based on PyTorch. In Proceedings of the 2022 IEEE 9th International Conference on Power Electronics Systems and Applications (PESA), Hong Kong, China, 20 September 2022; pp. 1–5.

27. Hansen, M.; Poddar, S.; Ahmed, H.; Kim, S.; Kamineni, A. Artificial Neural Network Modeling of WPT Magnetic Fields in an EV Application. In Proceedings of the 2023 IEEE Wireless Power Technology Conference and Expo (WPTCE), San Diego, CA, USA, 4 June 2023; pp. 1–6.

28. Sim, B.; Lho, D.; Park, D.; Jeong, S.; Lee, S.; Kim, H.; Park, H.; Kang, H.; Hong, S.; Kim, J. A Deep Neural Network-Based Estimation of Efficiency Enhancement by an Intermediate Coil in Automotive Wireless Power Transfer System. In Proceedings of the 2020 IEEE Wireless Power Transfer Conference (WPTC), Seoul, Republic of Korea, 15 November 2020; pp. 231–233.

29. Sim, B.; Lho, D.; Park, D.; Park, H.; Kang, H.; Kim, J. A Deep Neural Network-Based Estimation of EMI Reduction by an Intermediate Coil in Automotive Wireless Power Transfer System. In Proceedings of the 2020 IEEE International Symposium on Electromagnetic Compatibility & Signal/Power Integrity (EMCSI), Reno, NV, USA, 28 July–28 August 2020; pp. 407–410.

30. El-Sharkh, M.Y.; Touma, D.W.F.; Dawoud, Y. Artificial Neural Network Based Wireless Power Transfer Behavior Estimation. In Proceedings of the 2019 SoutheastCon, Huntsville, AL, USA, 11–14 April 2019; pp. 1–6.

31. Wu, Y.; Jiang, Y.; Li, Y.; Wang, C.; Wu, M.; Wang, N.; Wang, X.; Tang, Y. Precise Modeling of the Self-Inductance of Circular Coils with Deep Neural Networks. In Proceedings of the IECON 2023—9th Annual Conference of the IEEE Industrial Electronics Society, Singapore, 16 October 2023; pp. 1–7.

32. Gong, Y.; Otomo, Y.; Igarashi, H. Neural Network for Both Metal Object Detection and Coil Misalignment Prediction in Wireless Power Transfer. *IEEE Trans. Magn.* **2022**, *58*, 1–4. [CrossRef]

33. Liu, Y.; Liu, F.; Feng, H.; Zhang, G.; Wang, L.; Chi, R.; Li, K. Frequency Tracking Control of the WPT System Based on Fuzzy RBF Neural Network. *Int. J. Intell. Syst.* **2022**, *37*, 3881–3899. [CrossRef]

34. Yuan, X.; Xiang, Y.; Wang, Y.; Yan, X. Neural Networks Based PID Control of Bidirectional Inductive Power Transfer System. *Neural Process Lett.* **2016**, *43*, 837–847. [CrossRef]

35. Xiao, J.; Chen, S.; Wu, X.; Wang, Z.; Mo, Y. Position-Insensitive WPT System with an Integrated Coupler Based on ANN Modeling and Variable Frequency Control. In Proceedings of the 2022 IEEE 9th International Conference on Power Electronics Systems and Applications (PESA), Hong Kong, China, 20 September 2022; pp. 1–6.

36. Zhang, Z.; Yu, W. Communication/Model-Free Constant Current Control for Wireless Power Transfer Under Disturbances of Coupling Effect. *IEEE Trans. Ind. Electron.* **2022**, *69*, 4587–4595. [CrossRef]

37. Zheng, Z.; Wang, N.; Ahmed, S. Maximum Efficiency Tracking Control of Underwater Wireless Power Transfer System Using Artificial Neural Networks. *Proc. Inst. Mech. Eng. Part I J. Syst. Control Eng.* **2021**, *235*, 1819–1829. [CrossRef]

38. Li, Y.; Dong, W.; Yang, Q.; Zhao, J.; Liu, L.; Feng, S. An Automatic Impedance Matching Method Based on the Feedforward-Backpropagation Neural Network for a WPT System. *IEEE Trans. Ind. Electron.* **2019**, *66*, 3963–3972. [CrossRef]

39. Xu, J.; Tan, P.; Shen, H.; Zhang, H.; Pang, L.; Deng, Y. Angle Prediction for Field Orientation Based on Back Propagation Neural Network of Wireless Power Transfer System. In Proceedings of the 2020 IEEE 9th International Power Electronics and Motion Control Conference (IPEMC2020-ECCE Asia), Nanjing, China, 29 November 2020; pp. 1947–1951.

40. Cheng, Z.; Chen, H.; Qian, Z.; Wu, J.; He, X. Data-Enabled Estimation and Feedback Control Method Utilizing Online Magnetic Positioning System for Wireless Power Transfer Systems. In Proceedings of the 2020 IEEE Energy Conversion Congress and Exposition (ECCE), Detroit, MI, USA, 11 October 2020; pp. 5528–5531.

41. Tavakoli, R.; Pantic, Z. ANN-Based Algorithm for Estimation and Compensation of Lateral Misalignment in Dynamic Wireless Power Transfer Systems for EV Charging. In Proceedings of the 2017 IEEE Energy Conversion Congress and Exposition (ECCE), Cincinnati, OH, USA, 1–5 October 2017; pp. 2602–2609.

42. Jeong, S.; Lin, T.-H.; Tentzeris, M.M. A Real-Time Range-Adaptive Impedance Matching Utilizing a Machine Learning Strategy Based on Neural Networks for Wireless Power Transfer Systems. *IEEE Trans. Microw. Theory Technol.* **2019**, *67*, 5340–5347. [CrossRef]

43. Ferrouillat, P.; Guerin, C.; Meunier, G.; Ramdane, B.; Labie, P.; Dupuy, D. Computations of Source for Non-Meshed Coils with A–V Formulation Using Edge Elements. *IEEE Trans. Magn.* **2015**, *51*, 1–4. [CrossRef]

44. Meunier, G. (Ed.) *The Finite Element Method for Electromagnetic Modeling*; Wiley: London, UK; Hoboken, NJ, USA, 2008; ISBN 978-1-84821-030-1.

45. Binns, K.J.; Lawrenson, P.J.; Trowbridge, C.W. *The Analytical and Numerical Solution of Electric and Magnetic Fields*; Wiley: Chichester, UK, 1992; ISBN 0-471-92460-1.

46. Guerin, C.; Meunier, G. 3-D Magnetic Scalar Potential Finite Element Formulation for Conducting Shells Coupled with an External Circuit. *IEEE Trans. Magn.* **2012**, *48*, 323–326. [CrossRef]

47. Goodfellow, I.; Bengio, Y.; Courville, A. *Deep Learning*; Adaptive computation and machine learning; The MIT Press: Cambridge, MA, USA; London, UK, 2016; ISBN 978-0-262-03561-3.
48. Ioffe, S.; Szegedy, C. Batch Normalization: Accelerating Deep Network Training by Reducing Internal Covariate Shift. *arXiv* **2015**, arXiv:1502.03167.